AIAA SciTech
13-17 January 2014, National Harbor, Maryland
AIAA Atmospheric Flight Mechanics Conference

An Analytical Approach to Modeling Supersonic Retropropulsion Flow Field Components

Christopher E. Cordell, Jr.[1], and Robert D. Braun[2]
Georgia Institute of Technology, Atlanta, GA, 30332

The propulsive-aerodynamic interaction created by a vehicle employing supersonic retropropulsion results in a complex flow field where the bow shock forms in response to the effective obstruction created by the vehicle and the nozzle exhaust plumes. Wind tunnel and computational efforts provide high fidelity insight into these flow structures at the expense of a significant time investment for running simulations. Leveraging analytical techniques to model this flow field allows for more efficient exploration of the effects of supersonic retropropulsion and provides more information on expected interactions prior to utilizing higher fidelity approaches. This paper proposes a method for analytically determining plume structure and the resulting bow shock structure for single and three nozzle supersonic retropropulsion configurations. The single nozzle model is used to validate plume generation methods, and the three nozzle models are used to validate the full flow field structure, including both plumes and the bow shock. Computational simulations at zero angle of attack with a freestream Mach number of 2 show favorable correlation with the developed model.

Nomenclature

A_1, A_2	= nondimensional shock parameters
$A_{i,j}$	= matrix for solving source strengths
$\vec{A}$	= area vector, m^2
B	= axial density parameter
B_s	= bow shock bluntness
C	= barrel shock scaling parameter
C_i	= constant vector component
d	= distance from nozzle throat, m
d_{throat}	= throat diameter, m
dr	= differential radial distance, m
ds	= differential arc length, m
dx	= differential axial distance, m
$I_{1\text{-}5}$	= integral terms
$I_{i,j}$	= panel method integral
L_{cone}	= conical nozzle length, m
$\dot{m}$	= mass flow rate, kg/s
M	= Mach number
P	= static pressure, Pa
P_T	= stagnation pressure, Pa
r	= radial coordinate, m
r_{exit}	= nozzle exit radius, m
R_{ND}	= nondimensional radial coordinate
R_s	= bow shock nose radius, m
S_j	= panel length, m
V	= velocity magnitude, m/s
$\vec{V}$	= velocity vector, m/s
$V_{s,i}$	= surface velocity, m/s
V_{sub}	= velocity behind normal shock, m/s
x	= axial coordinate, m
x_b, x_c	= bow shock coordinates, m
X	= panel endpoint coordinate, m
X_0	= axial bow shock location, m
X_b, X_c	= bow shock coordinates, m
X_{ND}	= nondimensional radial coordinate
y	= panel centerpoint, m
Y	= panel endpoint coordinate, m
β_i	= panel orientation angle, rad
γ	= ratio of specific heats
η	= nondimensional bow shock coordinate
η_{body}	= nondimensional body axial location
θ_0	= initial jet expansion angle, rad
θ	= panel incidence angle to freestream, rad
λ	= panel source strength
ξ	= nondimensional bow shock coordinate
ρ	= density, kg/m^3
ρ_a	= jet shape function parameter
ρ_T	= total density, kg/m^3
φ	= jet shape function parameter
φ_{cross}	= crossflow deflection angle, rad
$\varphi(x,y)$	= panel velocity potential
ψ	= barrel shock constant

[1] Graduate Research Assistant, Guggenheim School of Aerospace Engineering, AIAA Student Member
[2] David and Andrew Lewis Associate Professor of Space Technology, Guggenheim School of Aerospace Engineering, AIAA Fellow

Subscripts

barrel	= barrel shock condition	$\parallel$	= parallel velocity vector
cross	= crossflow	$\perp$	= perpendicular velocity vector
i	= iterative counter	shock	= bow shock parameter
j	= iterative counter	terminal	= terminal shock condition
jet	= jet condition	∞	= freestream condition

I. Introduction

Supersonic retropropulsion (SRP) has been identified in the entry, descent, and landing (EDL) community as a potential deceleration technology for increasing performance of an entry system at Mars [1],[2]. SRP is characterized by an entry vehicle employing thrust to generate additional deceleration above and beyond that provided by aerodynamics alone during the supersonic phase of flight. By exhausting jet plumes into an oncoming supersonic freestream, a complex flow field is created due to the interactions between the plumes created by the nozzle exhaust and the bow shock required to decelerate the supersonic freestream flow. The presence of plumes within the flow field creates a larger effective obstruction than would exist for an entry vehicle with no SRP system. Understanding plume structure formation and its impact on the propulsive-aerodynamic interaction associated with SRP is critical to accurately evaluating the effects of vehicle and nozzle configuration on descent performance.

The current knowledge of the propulsive-aerodynamic interaction for SRP has primarily been derived from wind tunnel experiments and computational simulations. Many wind tunnel experiments for SRP have investigated the impact of a single nozzle located at the nose of a vehicle and flying at zero angle of attack [3]-[6]. For this configuration, the presence of a jet plume at the stagnation point of the vehicle results in a reduction of pressure across the forebody. As the thrust increases and the plume grows larger, more of the forebody is shielded from the oncoming freestream. The increase in thrust comes at the expense of a reduction in drag, meaning that nearly all of the deceleration force must be provided by the engine in this SRP configuration. Computational fluid dynamics (CFD) simulations of this configuration confirm this effect [7]-[9].

For a peripheral configuration, where multiple nozzles are utilized and positioned off the vehicle axis, a much different flow field is created. For lower thrust values, a high pressure stagnation region develops inboard of the plumes from each nozzle. This results in some degree of drag preservation in addition to the thrust provided by the engines [5]. This effect is dependent on how far from the vehicle axis the nozzles are located, as eventually the plumes will grow in size such that they interact and potentially coalesce with each other, creating a shielding of the forebody [6]. CFD simulations of a peripheral configuration confirm this flow behavior over a range of thrust conditions, noting that at low thrusts the plumes are small and independent of each other, while higher thrusts result in larger plumes that can create a coalesced plume structure [8]-[12].

Wind tunnel experiments are time and cost intensive to perform, which makes exploring a wide range of potential configurations difficult. While CFD approaches are capable of modeling a range of configurations at a lower cost, the significant computational resources required to capture SRP flow physics and time required to generate each solution can become problematic for large design space explorations. Leveraging analytical approaches to modeling SRP flow fields allows for configuration studies to be performed at a lower fidelity to down-select to configurations of interest for higher fidelity analysis. Additionally, knowledge of expected flow field structures for a range of vehicle and nozzle configurations provides more information prior to CFD analysis, allowing for more efficient grid generation because areas of interest will be highlighted for concentration of grid resolution. Jarvinen and Adams showed for a single nozzle configuration that piecewise modeling of the SRP flow field resulted in a good overall model of the entire flow structure [5]. By first modeling the plume structure [13],[14], then creating an effective obstruction to the freestream flow [15], and finally determining the resultant bow shock, it was shown that the full flow field could be approximated. Their efforts did not extend this analysis to the peripheral configuration. Recent work by Korzun [16], Bakhtian and Aftosmis [17], and Skeen [18] all attempted to model the aerodynamic drag caused by SRP configurations without explicitly modeling the flow field structure. Korzun assumed that multiple plumes coalesced into a single plume, which can only occur for certain thrust conditions on a given vehicle and nozzle configuration [16]. Bakhtian and Aftosmis assumed that SRP creates an oblique shock cascade forward of the vehicle; however, the formation of this shock cascade is not derived from an input SRP configuration [17]. Skeen examined a CFD solution for a single configuration at a single low thrust condition to define regions along the vehicle surface whose pressures are defined by varying flow assumptions, such

as the oblique shock cascade of Bakhtian and Aftosmis occurring between nozzles or modified Newtonian flow occurring near the stagnation region of the vehicle. However, the work by Skeen does not model the flow field structure directly [18]. Cordell and Braun [19] showed that independent plume flow for multiple nozzle configurations could be modeled by leveraging past analytical works for plume terminal shock location [20] and the plume boundary [14]. Flow conditions related to the SRP environment, including both jet flow and freestream conditions, allow for determination of relevant boundary conditions in the determination of the plume structure [19].

The work presented in this paper will extend the approach of Cordell and Braun [19] to create a modeling environment for generating full SRP flow field structures for peripheral configurations, including both plume and bow shock structures. For this analysis, it will be assumed that the vehicle is at zero angle of attack with a supersonic freestream. Plume interaction and coalescence is not modeled in this environment, as each plume is treated as an independent entity. Comparisons with relevant CFD simulations will be performed to validate the model for multiple SRP configurations.

II. Plume Structure

The plume terminal shock model used to determine extent of the plume away from the nozzle exit is identical to the method previously described by Cordell and Braun [19] as adapted from the work of Sibulkin and Gallaher [20]. The underlying basis equations for the plume barrel shock are also identical to the work of Cordell and Braun [19] as adapted from past work by Charwat [14]. Rather than perform a heuristic scaling of the barrel shock for each plume, a mass flow rate balance will be used to ensure that the flow out of the plume through the terminal and barrel shocks is equivalent to the input mass flow rate at the nozzle throat. A subsonic panel method as described by Anderson [22] will be adapted for the SRP environment to determine nominal surface pressure and velocity into which the plumes exhaust, which will serve as a basis for determining the deflection angle for a given plume due to exhausting into a local crossflow.

A. Overview of Plume Barrel Shock Equations

In the past work by Cordell and Braun, the method of Charwat was used to define the plume barrel shock shape function [19]. The nondimensional parameters for this method are given in Eq. 1 and Eq. 2, where θ_0 is the initial expansion angle of the flow out of the nozzle and ψ is a parameter defined in the Charwat approach to modeling the plume boundary [14]. Nondimensional axial and radial coordinates for the plume boundary are shown in Eq. 3 and Eq. 4 respectively, where r_{exit} is the exit radius of the nozzle. These two nondimensional coordinates are related to each other as shown in Eq. 5.

$$\rho_a = \sqrt{1 + \frac{\theta_0}{\psi}} \tag{1}$$

$$\varphi = \psi + \theta_0 \tag{2}$$

$$X_{ND} = \frac{x}{r_{exit}\rho_a} \tag{3}$$

$$R_{ND} = \frac{r}{r_{exit}\rho_a} \tag{4}$$

$$X_{ND} = \int_{1/\rho_a}^{R_{ND}} \cot\left[\varphi\left(1 - R_{ND}^2\right)\right] dR_{ND} \tag{5}$$

Comparison of the results from these equations with CFD solutions showed that the analytical plume barrel shock is narrower than is seen in computational simulations. Cordell and Braun proposed that a correction was

required to account for the fact that the plume exhausts into a stagnate flow rather than a vacuum, and provided a heuristic scaling factor based on the isentropic area ratio calculated for the terminal shock Mach number [19]. This method showed better agreement in predicting the plume boundary; however, the heuristic scaling is only validated against two configurations and is not necessarily extensible to other vehicles. Rather than rely on comparisons to computational or experimental results to determine if a heuristic scale factor is reasonable, this work proposes a different method to scale the plume barrel shock shape which is dependent on input flow conditions.

B. Mass Flow Rate Scaling

As an SRP jet does not exhaust into a purely quiescent environment as is assumed for the Charwat model, the base plume boundary shape function underpredicts the actual radius of the plume as a function of distance from the nozzle exit [19]. This disagreement is corrected by ensuring that the mass flow out of the plume boundary balances with the known input mass flow rate for a given thrust value for the nozzle. The Charwat model nominally assumes an infinitely long plume due to the presence of the cotangent function in Eq. 5. By truncating the plume at the calculated terminal shock location, some mass flow out of the plume boundary is lost, as shown in Fig. 1. This lost mass flow needs to be accounted for by calculating the mass flow rate through the terminal shock and combining that with the flow through the plume boundary to determine the total mass flow rate out of the plume. For this analysis, it is assumed that the Charwat approach gives an appropriate shape function for the plume boundary. The plume is then uniformly scaled, with a factor denoted as *C* in this work, such that the total mass flow rate out of the plume balances with the input conditions for the nozzle.

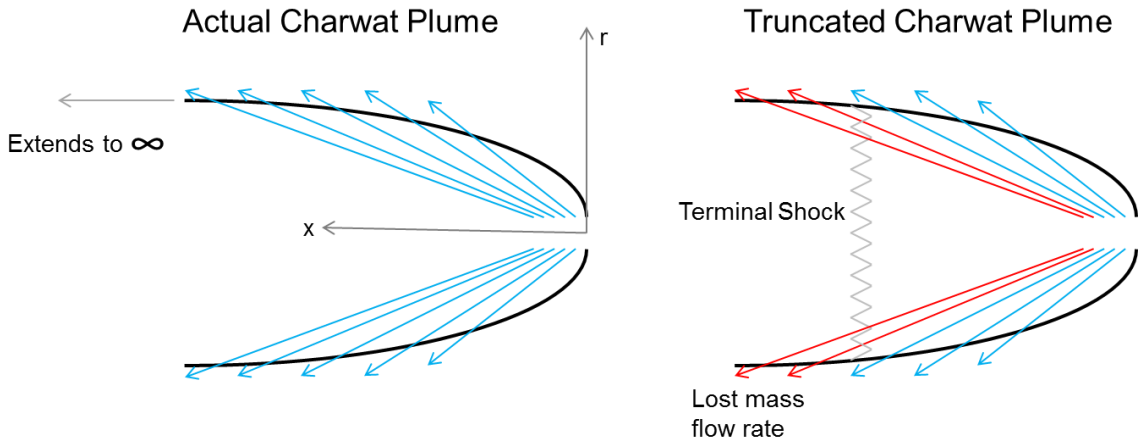

Figure 1. Comparison of boundary mass flow rate accounted (blue) and unaccounted (red) for between the nominal Charwat plume model and the truncated plume boundary

For the assumed terminal shock, the flow direction is set to be normal to the shock, as shown in Fig. 2. For the outward flow through the barrel shock, the flow direction at the shock is assumed to be defined along a radial extension from a virtual origin at the nozzle throat to each point along the barrel shock. As the plume is assumed to be axisymmetric in this analysis, these vectors can be treated three-dimensionally with a revolution of 360°. The density ratio along a radial streamline, as defined in prior work by Cordell and Braun [19] and shown in Eq. 6, is used to determine the Mach number and subsequent velocity and pressure for each point along the plume barrel shock.

$$\frac{\rho}{\rho_{T,jet}} = B\left(\frac{d}{d_{throat}}\right)^{-2} \tag{6}$$

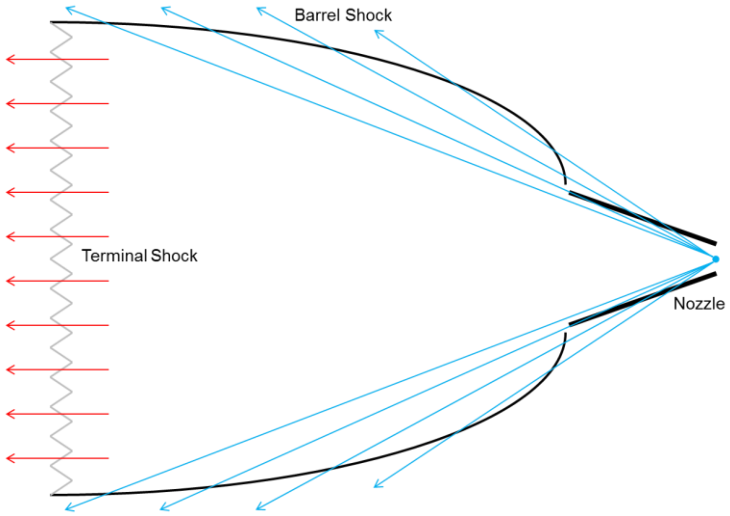

Figure 2. Vector representation of plume flow through the barrel shock (blue) and terminal shock (red)

There are three key assumptions for these flow directions through the plume boundaries. First is that the flow through the terminal shock is normal to the shock. As seen in Fig. 3 for a single nozzle, axisymmetric, CFD solution, the plume flow tends to expand and straighten to parallel the plume axis as it passes through the terminal shock. The second key assumption is that the direction of plume flow at the barrel shock can be represented with the virtual origin and the vectors shown in Fig. 2. This assumption is not implying that the actual flow path follows those vectors exactly, as that would require the jet flow to pass through solid boundaries of the nozzle for some locations. Rather, this assumption notes that the flow exiting the nozzle will initially expand outward, then turn prior to passing through the plume boundary. Figure 3 also shows this to be a reasonably accurate assumption far from the nozzle exit as the plume flow establishes itself.

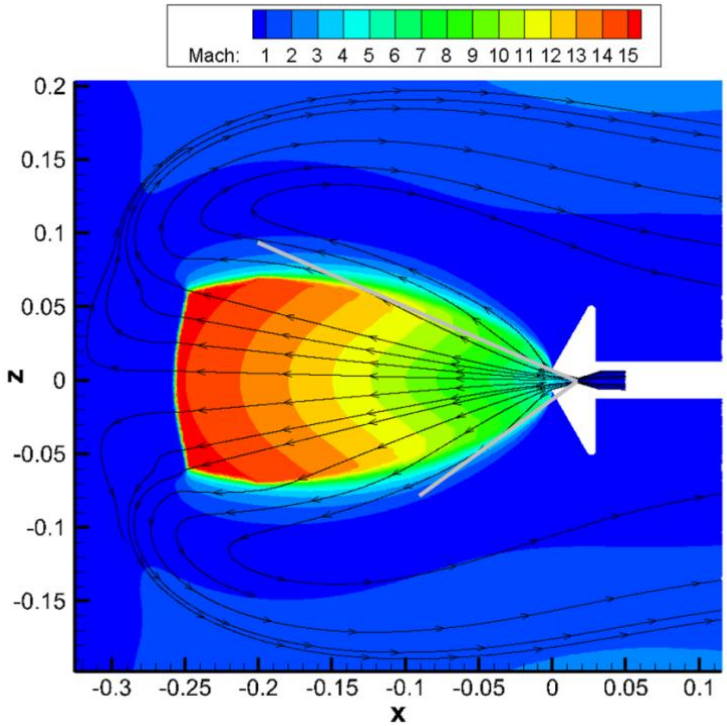

Figure 3. CFD solution with streamlines to show flow direction and two example tangent lines (gray) to these streamlines demonstrating reasonableness of nozzle throat assumption for determining flow direction at the barrel shock

The third key assumption requires the mass flow through the barrel shock near the exit to be insignificant. This is required to not violate the model assumptions since Fig. 3 shows that the flow has turned out of the nozzle and does not actually appear to emanate from the assumed point at the throat. Figure 4 shows a trend line of mass flow rate per unit area through the plume barrel shock as a function of distance from the nozzle exit for the CFD case shown in Fig. 3. It is observed that the mass flow rate for these locations is orders of magnitude smaller than for the remainder of the barrel shock. Thus the error in estimating the flow direction near the nozzle exit will not have a large impact on the total mass flow rate through the plume barrel shock.

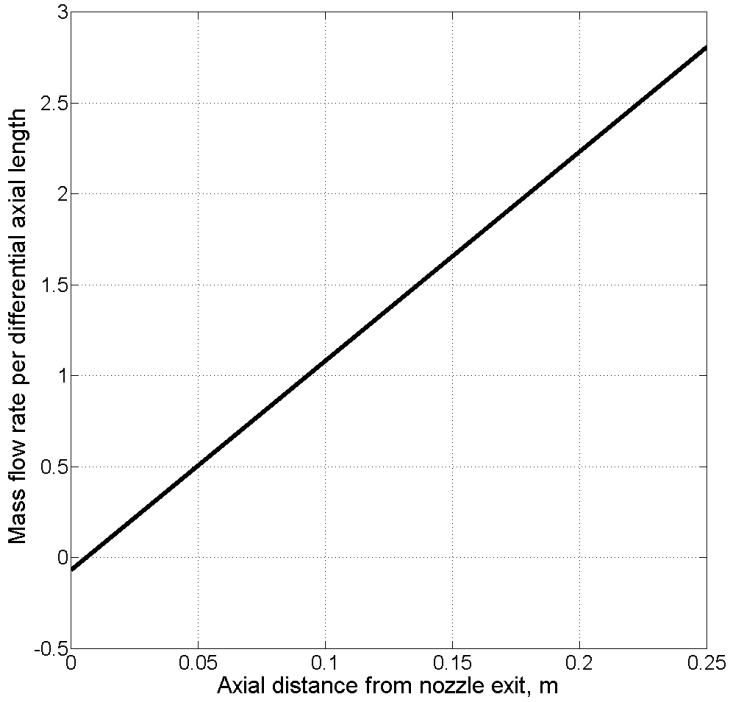

Figure 4. Mass flow rate per unit differential axial length trend line from single nozzle geometry CFD solution at C_T = 10

Traditionally, mass flow rate is calculated using Eq. 7 for a given density, velocity vector, and normal vector to a representative area. For the terminal shock, the flow is assumed to be normal to the shock with constant terminal shock conditions, so the mass flow rate reduces to that shown in Eq. 8.

$$\dot{m} = \rho\left(\vec{V} \cdot \vec{A}\right) \tag{7}$$

$$\dot{m}_{terminal} = \rho_{terminal} V_{terminal} \pi \left(Cr_{terminal}\right)^2 \tag{8}$$

For the flow through the barrel shock, the flow is assumed to pass through the shock in a direction defined as illustrated in Fig. 2. The distance from the center of the nozzle throat to a point along the plume barrel shock, denoted as *d* and calculated using Eq. 9, determines the flow conditions along the barrel shock as shown in Eq. 6. The Mach number at each point can be calculated using Eq. 10, which also sets the pressure ratio at each point. The speed of the flow at the barrel shock can then be calculated using Eq. 11.

$$d = \sqrt{\left(x + L_{cone}\right)^2 + \left(Cr\right)^2} \tag{9}$$

$$M_{barrel} = \sqrt{\frac{2}{\gamma - 1}\left[\left(\frac{\rho}{\rho_{T,jet}}\right)^{-(\gamma-1)} - 1\right]} \tag{10}$$

$$V_{barrel} = M_{barrel}\sqrt{\frac{\gamma P_{barrel}}{\rho_{barrel}}} \tag{11}$$

To determine the mass flow rate through each location along the plume barrel shock, the velocity direction and the normal vector to the shock need to be found. The velocity vector, being oriented along the line connecting the nozzle throat to a point on the shock, can be defined using Eq. 12. The area vector can be defined at a given point *i* using central numerical differencing as shown in Eqs. 13-15. Finally, the local mass flow rate can be revolved by 360° to account for the circular plume shape in three-dimensional space and summed over each point to get a total barrel shock mass flow rate as shown in Eq. 16.

$$\vec{V}_i = \frac{V_{barrel}}{d_i}\begin{bmatrix} x_i + L_{cone} \\ Cr_i \end{bmatrix} \tag{12}$$

$$dx_i = \frac{x_{i+1} - x_{i-1}}{2} \tag{13}$$

$$dr_i = \frac{r_{i+1} - r_{i-1}}{2} \tag{14}$$

$$\vec{A}_i = \frac{dx_i}{\sqrt{C^2 dr_i^2 + dx_i^2}}\begin{bmatrix} -C \cdot dr_i \\ dx_i \end{bmatrix} \tag{15}$$

$$\dot{m}_{barrel} = \sum_{i=2}^{N-1}\left(2\pi C r_i\right)\rho_i\left(\vec{V}_i \cdot \vec{A}_i\right) \tag{16}$$

C. Crossflow Deflection Angle

Because there can be a stagnation region inboard of a multiple nozzle configuration, a plume is effectively a jet in a local crossflow for this type of configuration. The strength of the crossflow depends on both the angle between the nozzle axis and the freestream flow vector and the angle between the nozzle axis and the surface of the vehicle. Both angles are needed as the direction of the freestream flow vector sets the stagnation point on the vehicle, and the incidence angle of the nozzle axis to the surface determines the relative angle of the surface flow to the jet flow. In addition to these orientation considerations, the physical cause of perturbations to a jet in crossflow is due to the static pressure, velocity, and stagnation pressure of the flow into which the nozzle exhausts. These effects manifest themselves across the entire length of the plume. Simplifying assumptions have been made in this model to account for these perturbations. First, the decelerated freestream flow which causes the crossflow deflection is assumed to always be parallel to the vehicle surface at the location where the nozzle intersects the vehicle. This is true near the surface, but not as valid in the flow field far from the vehicle where the flow reacts to the plume structure. Additionally, the static pressure contribution to the plume deflection is considered to be minimal, such that the primary driver of the crossflow deflection angle is the relative velocity of the decelerated freestream surface flow to the jet exit flow. This allows for vector relationships to be used to define the deflection angle. Lastly, the entire plume is assumed to rotate due to the local crossflow perturbations. In actuality, the pressure boundary condition that alters the plume structure varies as a function of the angular location around the plume, such that the inboard plume boundary has the largest perturbation while the outboard plume boundary is less disturbed. Attempting to

model this variable deflection effect requires knowledge of the flow as it passes around the plume obstruction, which is beyond the scope of this model.

To model the effects of crossflow on the plume structure, the numerical source panel method for nonlifting flows described by Anderson [22] is adapted for an SRP flow field. This method assumes a subsonic freestream flow with a distribution of sources and sinks defined piecewise along an arbitrary surface. The method returns a velocity at each point along the surface. To recreate the subsonic freestream, the flow behind the bow shock in the SRP flow field is used as a local effective freestream, assumed to be conditions caused by a normal shock to be consistent with prior assumptions in the analytical model. The velocity potential for this flow is given in Eq. 17 assuming a continuous body. The angle of attack here is assumed to be nearly zero, such that the stagnation point on the vehicle remains close to the nose. By breaking the body up into panels, the discrete form of the governing velocity potential can be found as shown in Eq. 18 for a given panel *i* based on the effects of every panel *j*. This form assumes the control point for each panel is the center of the panel. The distance from each control point is given in Eq. 19.

$$\phi(x,y) = \int_a^b \frac{\lambda ds}{2\pi} \ln(r) \tag{17}$$

$$\phi(x_i, y_i) = \sum_{j=1}^{N} \frac{\lambda_j}{2\pi} \int_j \ln(r_{ij}) ds_j \tag{18}$$

$$r_{ij} = \sqrt{(x_i - x_j)^2 + (y_i - y_j)^2} \tag{19}$$

Anderson describes a method for closed form solving Eq. 18 by applying the boundary condition that the normal component of the surface velocity is zero. This results in the general matrix form shown in Eq. 20, with components of the matrix *A* and vector *C* shown in Eq. 21 and Eq. 22 respectively. The integral term can be solved by using integral tables and defining intermediate variables in terms of the variables shown in Fig. 5, including the control point of each panel, the endpoints of each panel, and the incidence angle of the panel surface to the subsonic freestream. The panel being examined is panel *i* in this notation, while *j* represents another panel whose impact on panel *i* is being evaluated. Eq. 23 shows the intermediate variables, used to solve the integral term shown in Eq. 24. Finally, the surface tangent velocity can be solved using Eq. 25 for use in determining crossflow deflection angle.

$$[A_{i,j}][\lambda_j] = [C_i] \tag{20}$$

$$A_{i,j} = \begin{Bmatrix} \frac{\lambda_i}{2}, i = j \\ \frac{\lambda_j}{2\pi} I_{i,j}, i \neq j \end{Bmatrix} \tag{21}$$

$$C_i = -V_{sub} \cos \beta_i \tag{22}$$

$$\begin{bmatrix} I_1 \\ I_2 \\ I_3 \\ I_4 \\ I_5 \\ S_j \end{bmatrix} = \begin{bmatrix} -(x_i - X_j)\cos\theta_j - (y_i - Y_j)\sin\theta_j \\ (x_i - X_j)^2 + (y_i - Y_j)^2 \\ \sin(\theta_i - \theta_j) \\ (y_i - Y_j)\cos\theta_j - (x_i - X_j)\sin\theta_j \\ \sqrt{I_2 - I_1^2} \\ \sqrt{(X_{j+1} - X_j)^2 + (Y_{j+1} - Y_j)^2} \end{bmatrix} \tag{23}$$

$$I_{i,j} = \frac{I_3}{2}\ln\left(\frac{S_j^2 + 2I_1S_j + I_2}{I_2}\right) + \left(\frac{I_4 - I_1I_3}{I_5}\right)\left[\tan^{-1}\left(\frac{S_j + I_1}{I_5}\right) - \tan^{-1}\left(\frac{I_1}{I_5}\right)\right] \tag{24}$$

$$V_{s,i} = V_{sub}\sin\beta_i + \sum_{j=1}^{N}\frac{\lambda_j}{2\pi}\left[\left(\frac{I_4 - I_1I_3}{2I_5}\right)\ln\left(\frac{S_j^2 + 2I_1S_j + I_2}{I_2}\right) - I_3\left[\tan^{-1}\left(\frac{S_j + I_1}{I_5}\right) - \tan^{-1}\left(\frac{I_1}{I_5}\right)\right]\right] \tag{25}$$

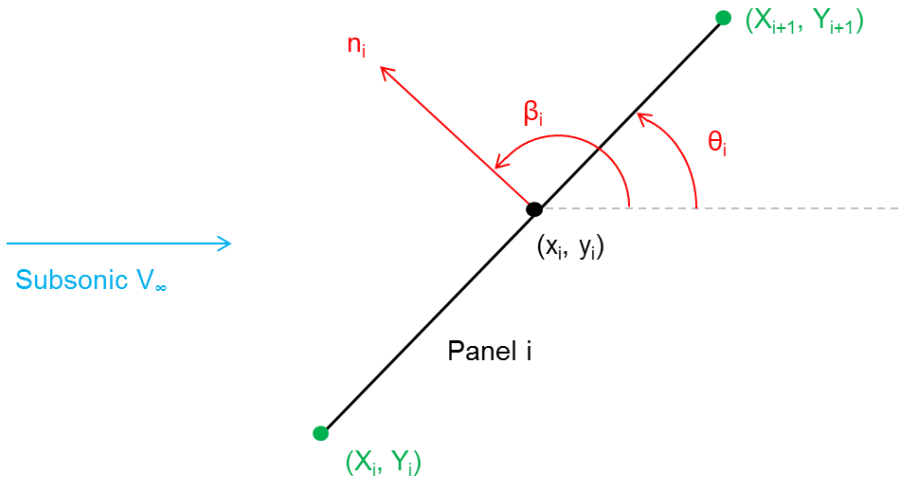

Figure 5. Schematic of a single panel with relevant points and angles for the subsonic panel method

Once the surface velocity that would exist without the presence of the plumes is known at the location of the nozzle exit, this is assumed to be the speed of the flow which causes the crossflow effects on the plume. This flow is assumed to emanate from near the nose, meaning that the flow velocity should always be directed outboard and causing the plume to turn away from the stagnation point. A velocity triangle is used to determine the deflection angle of the plume caused by the local crossflow, as shown in Fig. 6. The parallel velocity component is defined to be the component of the crossflow velocity in the direction of the jet exit velocity, as defined in Eq. 26. The perpendicular velocity is any velocity from the crossflow which does not flow along the jet exit velocity vector, as defined in Eq. 27. The crossflow angle of deflection can then be calculated using Eq. 28. To include the crossflow angle in the plume definition, the scaled barrel shock is rotated outboard by the crossflow angle about the intersection of the nozzle axis with the vehicle surface.

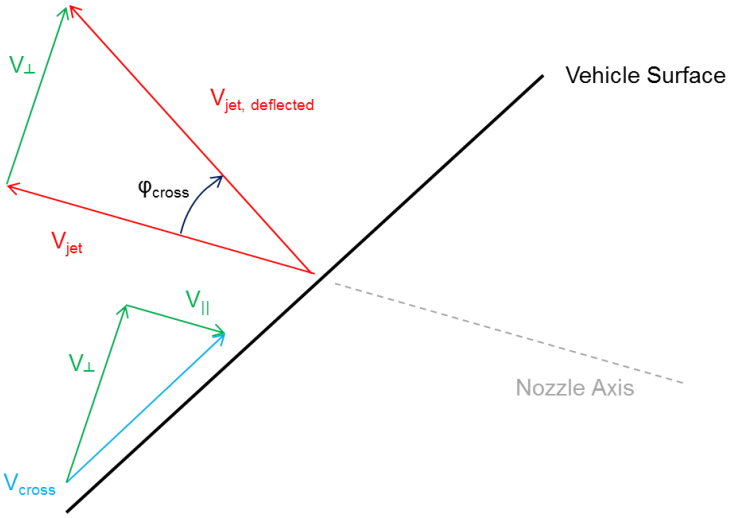

Figure 6. Schematic of the velocity triangle created to determine the crossflow deflection angle

$$\vec{V}_{\parallel} = \frac{\left(\vec{V}_{jet} \cdot \vec{V}_{cross}\right)\vec{V}_{jet}}{\left|\vec{V}_{jet}\right|^2} \tag{26}$$

$$\vec{V}_{\perp} = \vec{V}_{cross} - \vec{V}_{\parallel} \tag{27}$$

$$\phi_{cross} = \tan^{-1}\left(\frac{\left|\vec{V}_{\perp}\right|}{\left|\vec{V}_{jet}\right|}\right) \tag{28}$$

III. Bow Shock Structure

Supersonic flow will respond to blunt obstructions in the flow field by creating a bow shock to decelerate the flow to stagnation conditions forward of the obstruction. Nominally, the obstruction seen by the supersonic freestream consists of some vehicle; however, in the case of SRP, this obstruction consists of both the entry vehicle and the jet exhaust flow. Work by Van Dyke and Gordon [21] is used as the basis of the following analytical approach to modeling bow shock structure for SRP flow fields. The decelerated and turned plume flow is assumed to create a hemispherical obstruction for each nozzle in a configuration, which provides necessary geometry information to simplify Van Dyke's approach to modeling the bow shock. The method as presented here is applicable to multiple nozzle configurations where each nozzle is not located at the stagnation point on a vehicle.

A. Bow Shock Shape Equations

Van Dyke and Gordon assume that a two-dimensional bow shock (i.e. a cross section of an axisymmetric three-dimensional bow shock), can be functionally represented as a conic section [21]. The governing equation for such a surface is given in Eq. 29, where R_S is the nose radius of the shock and B_S is the bluntness. Van Dyke and Gordon go also propose a nondimensional, orthogonal coordinate system that contains the shock wave as one of the coordinate surfaces. The coordinate transforms between the nondimensional system (ξ, η) and the Cartesian system (x_{shock}, r_{shock}) are shown in Eqs. 30 and 31. In this formulation, the shock lies along $\xi = 1$, as shown in Fig. 7. The focus of the conic section lies at $\xi = \eta = 0$.

$$r_{shock}^2 = 2R_S x_{shock} - B_S x_{shock}^2 \tag{29}$$

$$\frac{x_{shock}}{R_S} = \frac{1}{B_S}\left[1 - \sqrt{\left(1 - B_S\xi^2\right)\left(1 - B_S + B_S\eta^2\right)}\right] \tag{30}$$

$$\frac{r_{shock}}{R_S} = |\xi|\eta \tag{31}$$

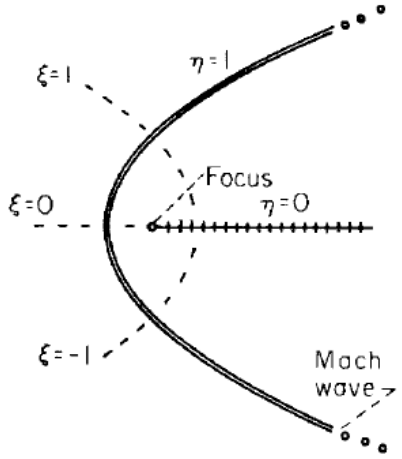

Figure 7. Shock aligned coordinate system used for bow shock definition [20]

Van Dyke and Gordon describe a numerical finite difference scheme which propagates the flow from an assumed shock shape until the surface of the body can be defined along each constant ξ line. For a range of freestream Mach numbers, shock shape, and γ values, results are tabulated to determine the bluntness of the body that would create each assumed shock structure. While the results are sparse over the entire set of all possible variable combinations, many of the results are reported for body bluntness equal to unity [21]. This would indicate a circular body in the two-dimensional sense, or a hemisphere in three-dimensional space.

B. Effective Hemispherical Obstruction

For a multiple nozzle SRP configuration, each plume will create its own local obstruction to the freestream flow. Each plume's flow will decelerate through the terminal shock then turn outboard relative to the stagnation point on the vehicle. For an axisymmetric vehicle at zero angle of attack, as will be assumed in this analysis, the stagnation point will be located at the nose of the vehicle. If no plume is present, the freestream flow will decelerate then appear to radiate outward from the stagnation point, creating an effective crossflow along the body. This local crossflow and the high pressure stagnation region inboard of the plumes cause the decelerated jet flow to turn outward. Using the plume boundary model described previously, each nozzle will have its own plume which is assumed not to interact with any other plumes that may be created by other nozzles. The center of the effective hemispherical obstruction for each plume will be set to the outermost point on the jet terminal shock, as measured radially from the nose. This is shown in Fig. 8. The radius of the hemispherical obstruction will be set to the diameter of the terminal shock to represent that all flow through the plume must react to the presence of the decelerated freestream and turn outboard.

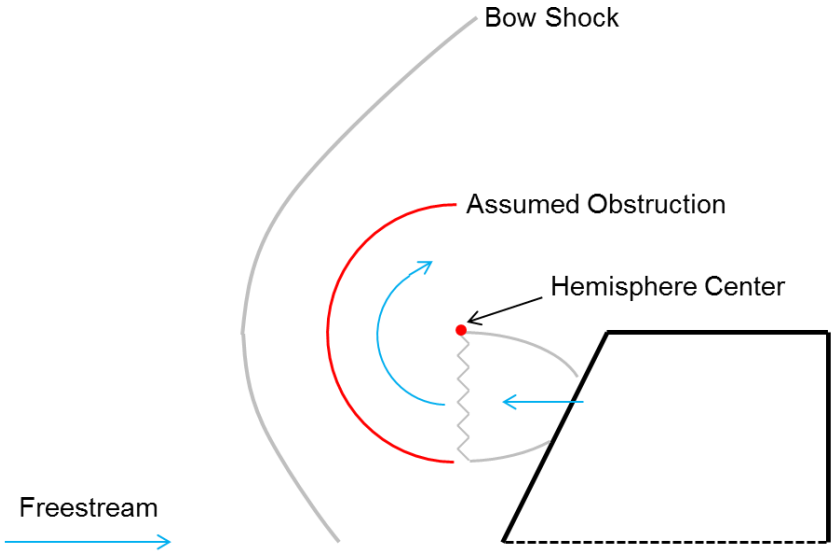

Figure 8. Two-dimensional illustration of the location for the hemispherical center and the definition of the assumed obstruction relative to this center point

C. Calculating 3-Dimensional Bow Shock

Definition of the local shock structure using Eqs. 30 and 31 requires knowledge of B_S, R_S, ξ, and η to solve for x_{shock} and r_{shock}. The shock bluntness term is found by interpolating Van Dyke and Gordon's reported data for a hemispherical obstruction for an input freestream Mach number and γ. Along the shock, it is known that $\eta = 1$, and ξ can be varied to calculate the distribution of the bow shock through Cartesian space. Rather than perform the numerical integration of Van Dyke for the entire bow shock structure, the assumption of a hemispherical obstruction means that only the flow along $\xi = 0$ needs to be solved to determine R_S. The geometry for this calculation is shown in Fig. 9.

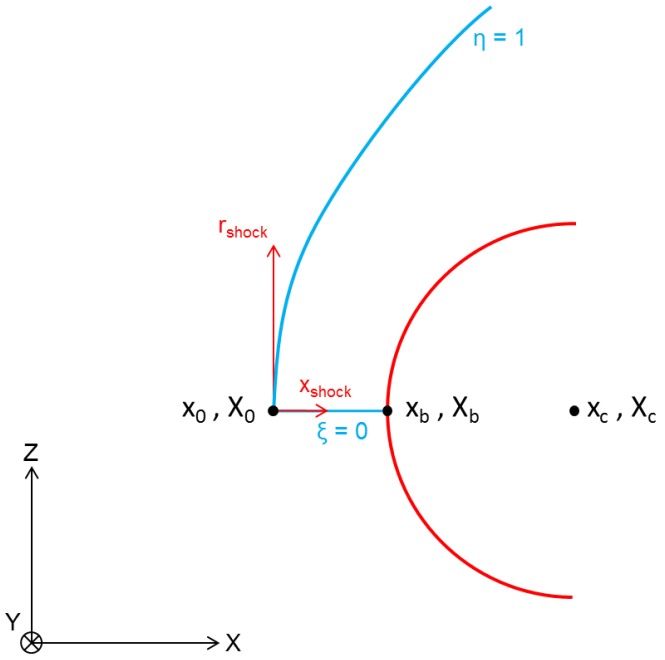

Figure 9. Nondimensional coordinate system (blue), Cartesian shock space (red), and actual dimensional coordinate system (black) with key axial points for determining shock nose radius

In the nondimensional coordinate system (ξ, η), η = 1 for the shock and ξ = 0 along the axis are known. Unknown in this frame is η_{body}, which specifies the nondimensional location of the hemispherical obstruction along the axis. This parameter can be calculated using the equations of motion specified by Van Dyke and Gordon, and performing a single integration along the axis. In the Cartesian shock space (x_{shock}, r_{shock}), the origin is at the intersection of the shock with the axis. In this space, x_0 is known to be zero, while x_b and x_c are unknown. In the actual dimensional coordinate system (X, Y, Z), within which the vehicle and plume structures are defined, the location of the focus, X_c, is known to be the center of the hemisphere found previously. The distance between this point and the hemisphere is equal to the diameter of the terminal shock, which means that X_b is known. The only unknown in this coordinate system is X_0, which would be the actual standoff location of the bow shock forward of the local obstruction provided by the decelerated and turned jet flow. The final unknown, R_S, is a function of these unknowns.

The coordinate transform in Eq. 30 and some geometrical relationships provide enough information to solve for all of the unknown variables in this problem. Eqs. 32 and 33 show applications of Eq. 30 to calculate the points x_c and x_b as functions of R_S along the axis, denoted as A_1 and A_2 respectively. The relationship shown in Eq. 34 can be used to determine R_S. Lastly, Eq. 35 is used to calculate X_0, which allows for the shock structure to be positioned in the actual dimensional coordinate system relative to the vehicle and plume structures.

$$A_1 = \frac{x_c}{R_S} = \frac{1}{B_S}\left(1 - \sqrt{1 - B_S}\right) \tag{32}$$

$$A_2 = \frac{x_b}{R_S} = \frac{1}{B_S}\left(1 - \sqrt{1 - B_S + B_S \eta_{body}^2}\right) \tag{33}$$

$$\left|X_b - X_c\right| = \left|x_b - x_c\right| = R_S \left|A_2 - A_1\right| \tag{34}$$

$$\left|X_0 - X_c\right| = \left|x_0 - x_c\right| = \left|x_0 - R_S A_1\right| \tag{35}$$

To generate the three-dimensional bow shock structure, the two-dimensional shock outline is first calculated by varying ξ along the shock and calculating x_{shock} and r_{shock}. The two-dimensional profile is then revolved by 360° about the local shock axis to create a local three-dimensional shock structure. This process is performed for each plume, and then combined into one global shock structure. This is done by assuming that the furthest offset shock from the vehicle at a given radial location and rotation angle about the vehicle axis is the dominant shock and will be the only shock present in the flow. No shock interactions are modeled, as the bow shock should appear to be one continuous shock structure. The intersection of bow shocks is treated in this continuous, but not necessarily differentiable, manner to transition from one local shock to another.

IV. Flow Field Structure Comparisons with CFD

The analytical model described in Section III has been validated against five geometries in this work. Two geometries are derived from the Jarvinen and Adams wind tunnel experiment [5] and compared against CFD solutions at varying thrust coefficient. The single nozzle configuration is primarily used to validate the approach for modeling plume structure, as this configuration exhibits an axisymmetric plume. The three nozzle configuration will compare the entire flowfield structure, including both the plume barrel shock and the bow shock. In addition to these two geometries, three configurations with three nozzles at varying nozzle cant angles are also investigated. These configurations have the same nozzle design as the wind tunnel derived, 0° nozzle canting, three nozzle configuration, maintaining an identical intersection point between the nozzle axis and the forebody as well as the same nominal exit radius at this point. Cant angles of 10°, 20°, and 30° are investigated to vary the relative angle between the nozzle exit flow and the oncoming freestream. All CFD solutions used as validation for the analytical model have been generated using FUN3D to solve steady state, calorically perfect gas equations. The simulations all assume turbulent flow with the Menter-SST turbulence model. The freestream flow for all configurations is identical, with M_∞ = 2, T_∞ = 173.4 K, and P_∞ = 1762.3 Pa. The nozzle inlet temperature is held constant at $T_{T,jet}$ =

294 K, and the nozzle inlet pressure ratios for varying thrust coefficient (C_T) are shown in Table 1 for both the single nozzle and three nozzle geometries.

Table 1. Nozzle plenum inflow conditions for varying geometry and thrust coefficient

Single Nozzle Geometry		Three Nozzle Geometries	
C_T	$P_{T,jet}/P_\infty$	C_T	$P_{T,jet}/P_\infty$
1.05	1581.2	1.0	1504.0
4.04	6060.2	4.0	6166.5
7.00	10494.2	7.0	10678.7
10.00	14988.2	10.0	15040.4

A. Single Nozzle Plume Structure

To investigate the performance of mass flow rate scaling on the plume structure, a comparison of the plume radius at the terminal shock location is shown in Fig. 10. The CFD simulations do not have a sharp barrel shock, but rather a barrel shock and free shear layer that form in the flow field. Thus, there is a thickness associated with the computational solutions that is represented in the plot as an upper and lower bound. These bounds have been extracted from the CFD solutions by probing Mach contours. The lower bound represents the approximate boundary between the core plume flow and the transition through the barrel shock. The upper bound represents the outermost boundary between the plume flow and the recirculation region that forms for the single nozzle configuration. The lower CFD boundary is most equivalent to the barrel shock boundary calculated in the generation of the analytical plume structure.

For the low thrust solutions, where the plume is elongated, the free shear layer is thin and the analytical model agrees well with the upper bound of the CFD simulations. Even though these plume structures do not exhibit a distinct terminal shock, the mass flow rate scaling approach is still able to capture the maximum plume radius seen in the CFD solutions. For the higher thrust cases, where the plume structure exhibits a terminal shock, the analytical model consistently falls between the lower and upper bounds. As thrust increases, the shear layer grows larger and the spread between the bounds increases. The analytical model tends to approach the lower bound of the CFD data, which should occur since that bound is approximately taken to be the location of the barrel shock and the barrel shock is what is being modeled in the analytical method.

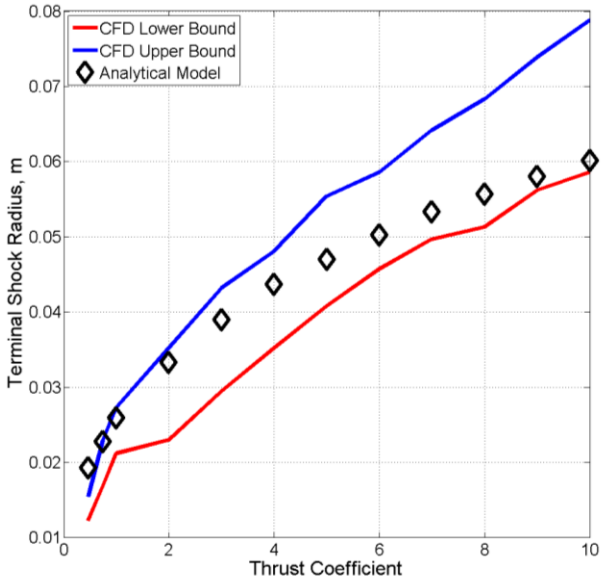

Figure 10. Comparison of terminal shock radius between CFD and analytical model for single nozzle configuration

A comparison of the full plume is shown in Fig. 11 for four thrust coefficients. As expected, the C_T = 1.05 analytical solution shows a significant underprediction of the extent of the plume due to this thrust level exhibiting a plume without a distinct terminal shock. For the analytical model, there is a consistent overprediction of the plume radius as a function of the distance along the plume axis compared to the CFD simulation near the nozzle exit. As thrust increases and the plume extends further upstream, the analytical prediction of the barrel shock slightly underpredicts the radius, as seen for C_T = 10. For higher thrusts, the initial expansion from the nozzle exit is well predicted by the scaled barrel shock of the analytical model. The computational solutions show a plume which increases in radius as the flow expands, then contracts prior to passing through the terminal shock. This behavior is not captured in the analytical model, which assumes a monotonically increasing plume radius with distance from the nozzle exit. Overall, the analytical model agrees well with CFD simulations in capturing the terminal shock radius and the initial plume expansion, while underpredicting the maximum plume expansion.

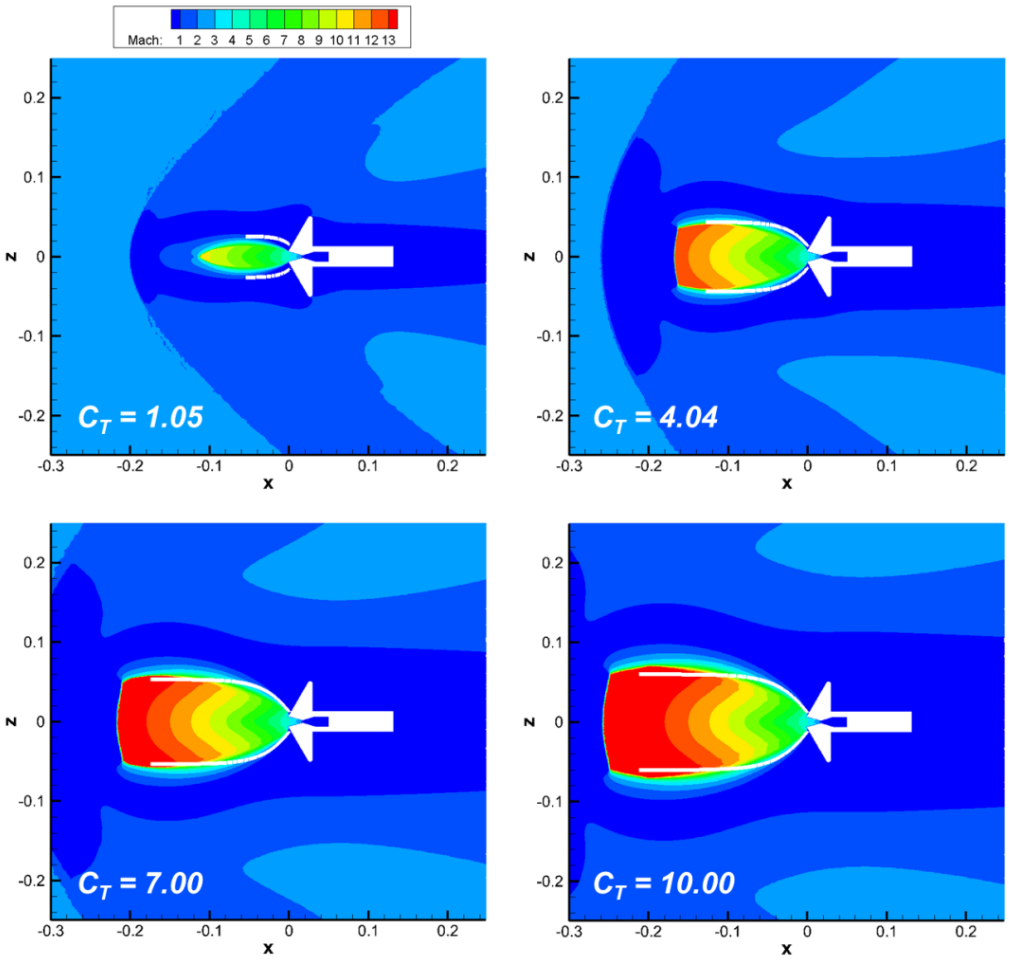

Figure 11. Comparison of single nozzle plume structures for CFD simulations and analytical model (white)

B. Three Nozzle Plume Structure

Flowfield structure predictions of the analytical model for a three nozzle configuration with zero degree nozzle canting, as is seen in the wind tunnel experiment performed by Jarvinen and Adams [5], are compared to CFD solutions in Fig. 12. These solutions include the crossflow deflection angle calculation for perturbing the plume structure as well as the predicted overall bow shock structure created by combining the local bow shocks for each plume. For C_T = 1, the outboard plume structure agrees well, as the crossflow angle for this configuration is only 7.1°. The inboard barrel shock is overpredicted; however, the rotation of the plume outboard directs the analytical plume in more of the correct direction due to crossflow effects. Increasing to C_T = 4 results in a barrel shock with

better inboard agreement across the entire analytical boundary, while the outboard barrel shock is slightly overpredicted. Further increasing to C_T = 7 shows good agreement for both plume boundaries. The inboard plume expansion is well captured, particularly the expansion of the plume near the nozzle exit. As the CFD plume structure becomes more complex, particularly because there is not a distinct terminal normal shock, the analytical model overpredicts the barrel shock inboard of the nozzle axis. The crossflow angle causes the analytical plume flow to be directed more outboard for all three of these thrust coefficients, consistent with the results seen in the CFD solutions.

While the extent of the plume for C_T = 10 is underpredicted due to the coalescence of the plumes, the outboard barrel shock shows a similar behavior as if the crossflow angle is still impacting the plume shape. The inboard barrel shock is well captured near the nozzle exit for this thrust condition, while the coalescence eventually results in the analytical model underpredicting the plume shape. This is a direct result of the analytical model being unable to capture the flow structure when the plumes coalesce, as the model assumes each plume to be independent of all other plumes.

The crossflow deflection angle causes an outboard shift in the effective obstruction for each plume, as the hemisphere center is set to be the furthest extent of the outboard barrel shock. For C_T = 1, 4, and 7, this results in a consistent overprediction of the bow shock standoff distance forward of the plume. However, the inboard standoff distance, while still overpredicted, is closer to the CFD solution than is seen if no crossflow angle is considered. For C_T = 10, the bow shock structure is underpredicted since the analytical model does not take into account the increase in plume axial extent due to plume coalescence.

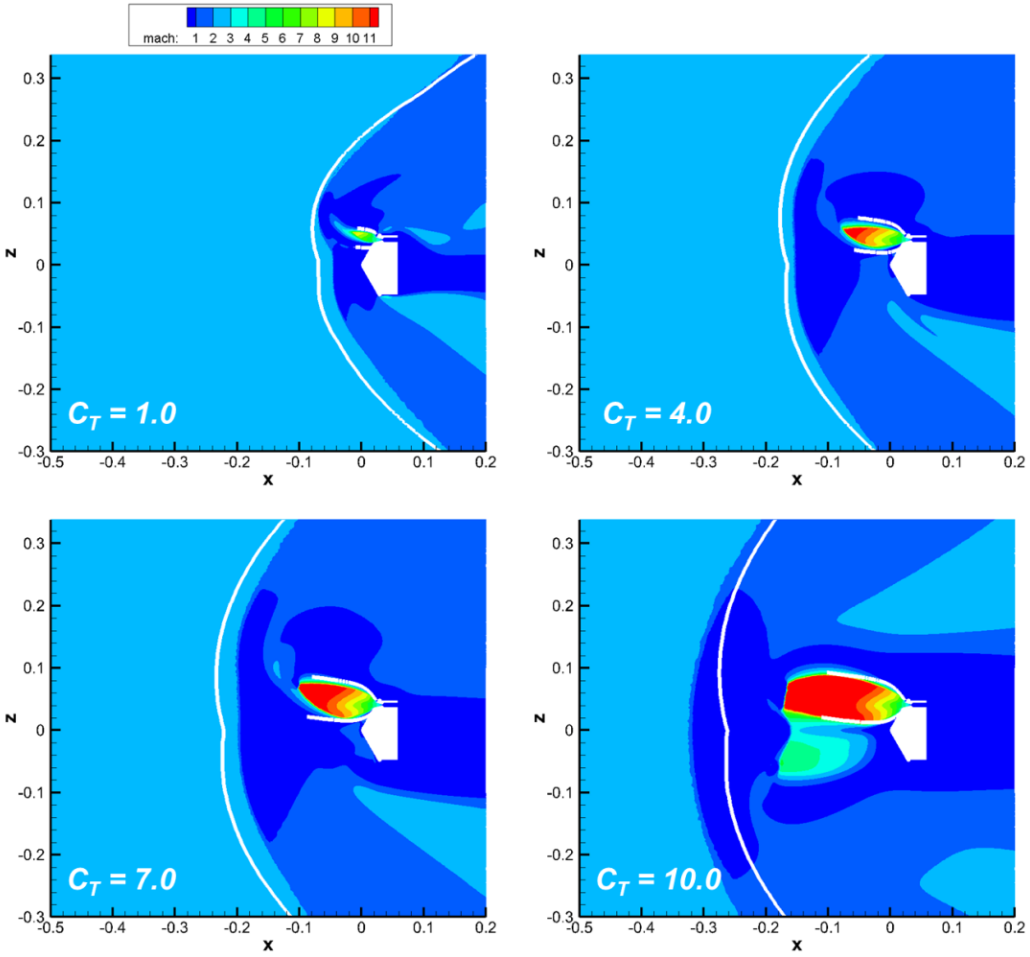

Figure 12. Comparison of three nozzle plume structures for CFD simulations and analytical model (white)

C. Effect of Forebody Nozzle Canting

For a 10° nozzle cant angle, the comparisons of the analytical model with CFD Mach contours for varying C_T values at zero angle of attack are shown in Fig. 13. For all thrust coefficients, the bow shock standoff distance is overpredicted by the analytical model, consistent with the results seen for the geometry with no nozzle canting when the plumes did not coalesce. This is due to a difference between the assumed obstruction shape of a hemisphere and the actual obstruction created by the jet plume. For this low nozzle cant angle, the barrel shock agrees well with the CFD solution. The analytical plume flow velocity has the same direction as the computational plume, with the outboard barrel shock agreeing well across the entire plume. The inboard barrel shock overpredicts the plume expansion, as the analytical model assumes an axisymmetric plume even when the crossflow angle is considered. The actual flow field shows an asymmetric plume, which is not captured in the assumptions of the model. The crossflow angle determined for this configuration is larger than for the zero nozzle canting geometry, with a calculated angle of 7.7°. The larger crossflow angle is due to the increase in relative angle of the jet exit flow to the local crossflow.

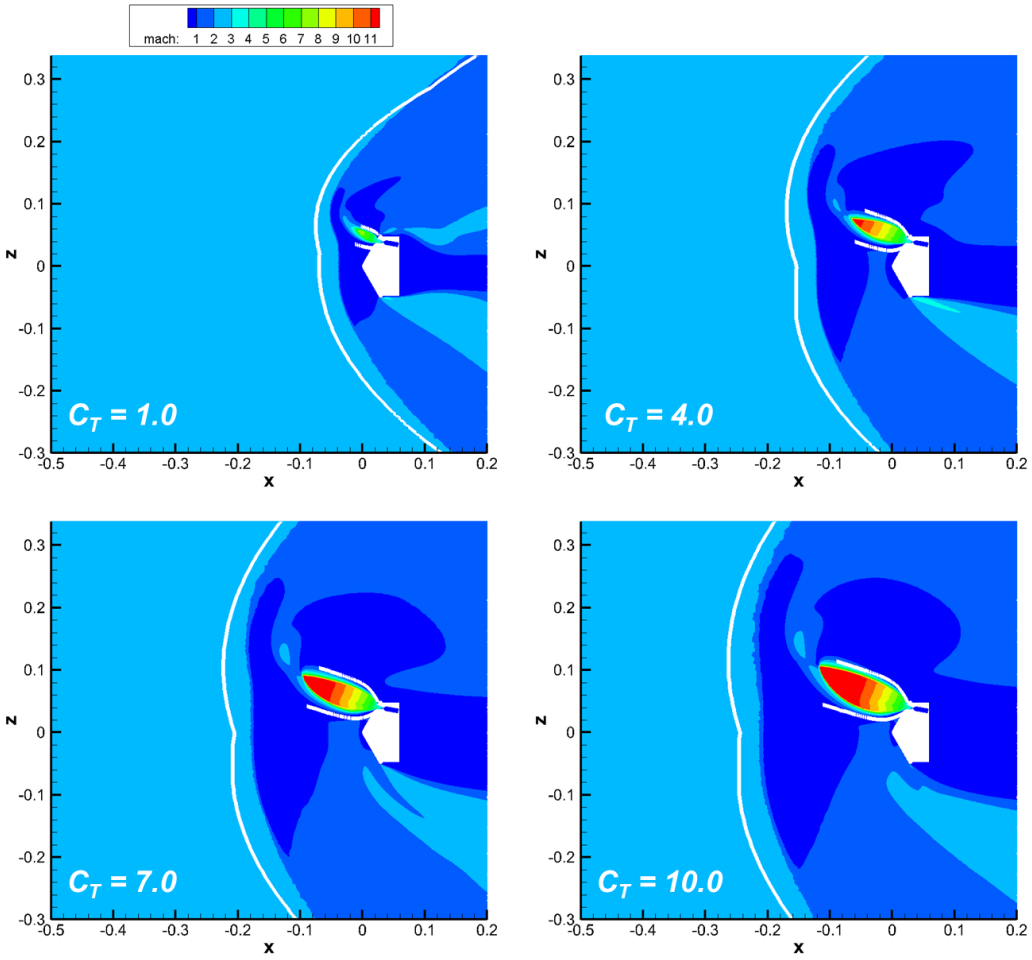

Figure 13. Comparison of three nozzle plume structures for 10° nozzle canting

Comparisons for C_T = 1, 4, 7, and 10 are shown in Fig. 14 for the 20° nozzle canting configuration at zero angle of attack. The stagnation point for these conditions is located at the nose of the vehicle, and the relative orientation of the nozzle exit flow to the surface is more normal than for the 10° nozzle canting configuration. While the crossflow deflection angle calculated in the analytical model increases as expected, to a value of 8.0°, this is not sufficient to capture the CFD plume boundaries as well as in the lower cant angle solutions. The inboard barrel shock is significantly overpredicted across all thrust coefficients. The outboard barrel shock is underpredicted,

particularly for the larger C_T values of 7 and 10. The initial expansion is well captured, and the low thrust condition of C_T = 1 shows good agreement across the entire plume structure due to the small plume created at this thrust level. The radial extent of the plume is underpredicted by the analytical model, as the crossflow angle does not sufficiently perturb the plume structure outboard. Since the analytical model creates a plume which is directed more upstream than the CFD solutions, the resulting bow shock standoff distance is significantly overpredicted as the effective obstruction forms further upstream. The presence of a local perturbation to the bow shock structure forward of the nozzle for all C_T values is captured by the analytical model, even if the exact location is not accurately captured.

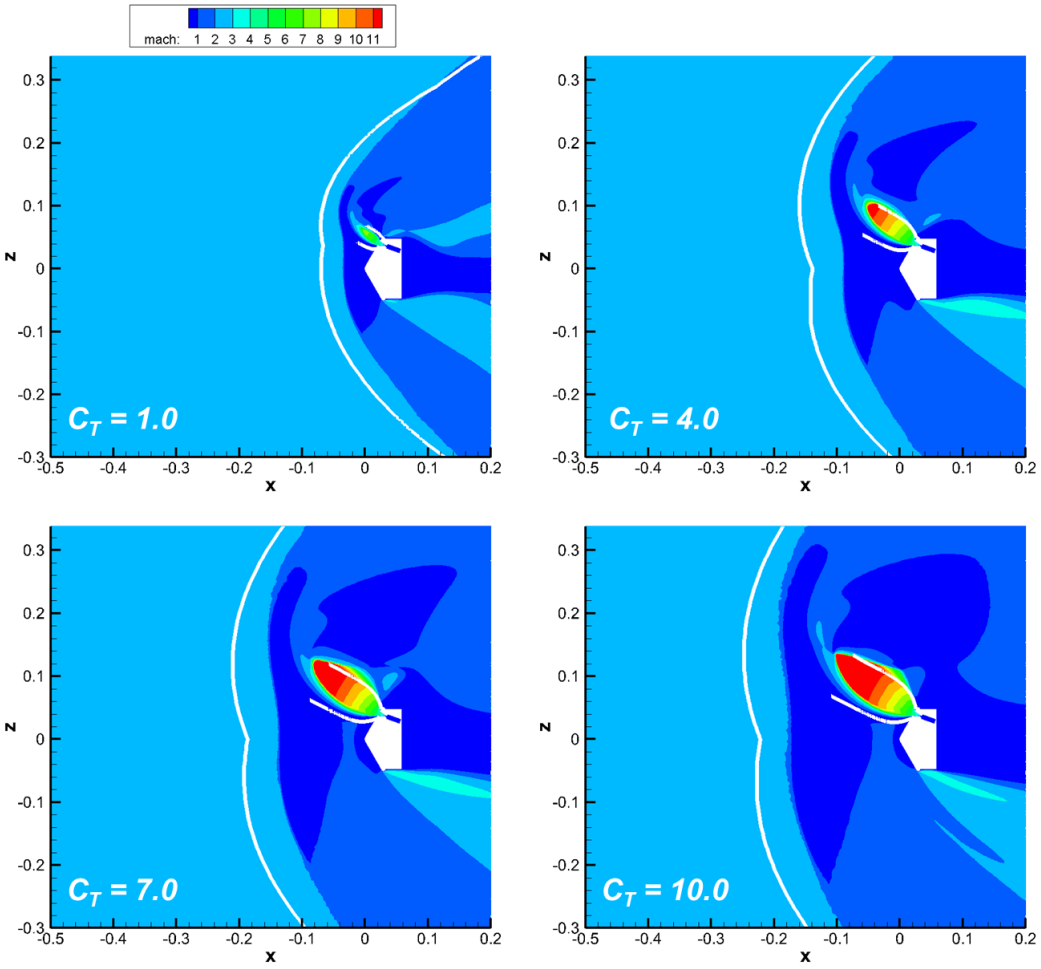

Figure 14. Comparison of three nozzle plume structures for 20° nozzle canting

Further increase in the nozzle cant angle to 30° shows more discrepancy between the analytical plume model and the CFD Mach contours for zero angle of attack solutions, as shown in Fig. 15. The nozzles in this configuration exhaust perpendicular to the vehicle surface, which causes the calculated crossflow angle to increase to 8.2°. For C_T = 1, the small plume structure still agrees well between the analytical model and the CFD solution. The inboard barrel shock overpredicts the expansion of the plume in that direction. The radial extent of the plume is underpredicted, as the calculated crossflow angle is not sufficient to rotate the plume enough to match the full radial extent. For the higher thrust conditions, the underprediction of the outboard barrel shock by the analytical model is significant. The CFD solutions show a crossflow deflection angle much larger than is calculated in the analytical model, and the plume expansion extends to a greater distance from the nozzle exit than the terminal shock assumption of the model captures. The inboard barrel shock shows the same consistent overprediction of the inboard expansion, resulting in an accurate capture of the axial extent of the plume structure. As the plume is directed more upstream in the analytical model than the CFD solutions, the resulting analytical bow shock also shows a larger standoff distance.

One cause of the discrepancy in the plume structure has to do with the interaction of the CFD plume structure with the separated flow at the shoulder of the vehicle, which perturbs the outboard barrel. Another cause of the discrepancy is the analytical approach to modeling crossflow deflection angle. The comparisons show that the crossflow angle should be a constant value for a given thrust condition, as the plume deflection appears to be a constant rotation about the intersection of the nozzle axis with the vehicle forebody. However, this angle is significantly underpredicted by the analytical model. The effect of the relative angle of the nozzle exit flow to the local surface flow direction is accounted for in the model, indicating that the assumption of a velocity triangle providing the crossflow deflection angle breaks down as the crossflow effect increases. An increase in crossflow deflection in the analytical model would direct the plume more outboard, causing the bow shock to form closer to the vehicle with the local shock perturbation further outboard.

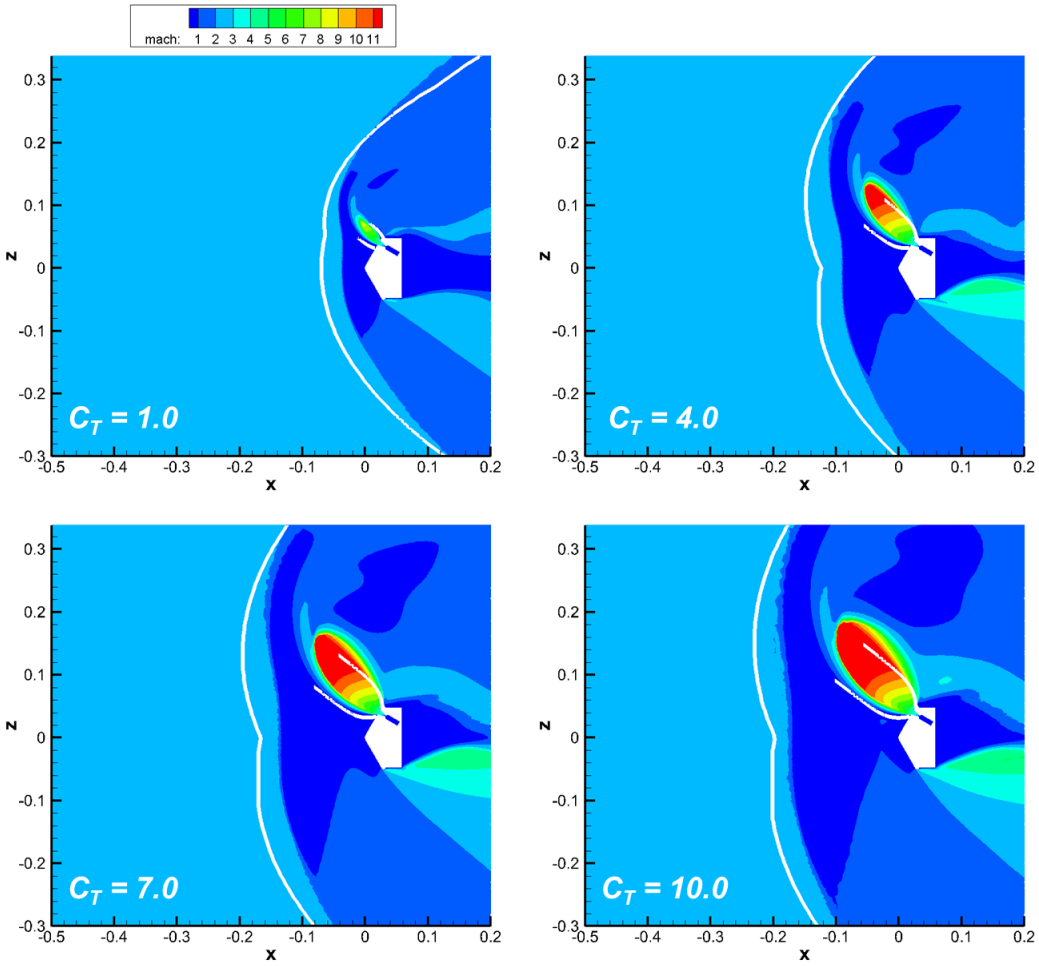

Figure 15. Comparison of three nozzle plume structures for 30° nozzle canting

V. Conclusions

For all five validation configurations, the analytical model is capable of capturing the maximum radial and axial extents of the plume structure, even if the predicted boundary does not precisely follow the Mach contours in the CFD solutions. For the single nozzle configuration, comparisons across multiple thrust coefficients show that scaling the plume barrel shock shape such that the mass flow rate out of the plume is equivalent with what is input at the nozzle throat provides a reasonable plume structure when compared with CFD solutions. For the three nozzle geometries, the crossflow deflection angle agrees well for configurations where the incidence angle between the nozzle axis and surface is small, and becomes less accurate as the nozzle exhausts more normal to the surface. The

bow shock for all configurations and conditions with independent plume structures consistently overpredicts the shock standoff distance from the vehicle.

If the nozzle exhausts nearly normal to the surface, such as for the 30° nozzle canting configuration, then the crossflow model is not valid and underpredicts plume perturbation. Configurations with lower incidence angles between the nozzle axis and the vehicle surface, such as the 0° and 10° nozzle canting configurations, show that the velocity triangle approach to modeling crossflow deflection is most valid for modeling plume perturbations. The analytical model is not valid for conditions where plume coalescence occurs, as the model assumes each plume expands independently of each other. The underprediction of plume structure for these configurations also causes an underprediction in bow shock structure for coalesced plumes. For all other configurations, the hemispherical obstruction is valid in terms of shape, though the center of the hemisphere is further outboard in the CFD solutions than is modeled in the analytical approach.

References

[1] Braun, R.D., and Manning, R.M., "Mars Exploration Entry, Descent, and Landing Challenges," *Journal of Spacecraft and Rockets*, Vol. 44, No. 2, 2007, pp. 310-323. doi: 10.2514/1.25116

[2] Adler, M., Wright, M., Campbell, C., Clark, I., Engelund, W., and Rivellini, T., "Entry, Descent, and Landing Roadmap Technology Area 09," NASA, November 2010.

[3] McGhee, R.J., "Effects of a Retronozzle Located at the Apex of a 140° Blunt Cone at Mach Numbers of 3.00, 4.50, and 6.00," NASA TN D-6002, January 1971.

[4] Love, E.S., and Grigsby, C.E., "Some Studies of Axisymmetric Free Jets Exhausting from Sonic and Supersonic Nozzles into Still Air and into Supersonic Freestreams," NACA RM-L54L31, May 1955.

[5] Jarvinen, P.O., and Adams, R.H., "The Aerodynamic Characteristics of Large Angled Cones with Retrorockets," NAS 7-576, February 1970.

[6] Berry, S.A., Rhode, M.N., Edquist, K.T., and Player, C.J., "Supersonic Retropropulsion Experimental Results from the NASA Langley Unitary Plan Wind Tunnel," AIAA Paper 2011-3489, June 2011.

[7] Korzun, A.M., Cordell, C.E. Jr., and Braun, R.D., "Comparison of Inviscid and Viscous Aerodynamic Predictions of Supersonic Retropropulsion Flowfields," AIAA Paper 2010-5048, July 2010.

[8] Cordell, C.E. Jr., Clark, I.G., and Braun, R.D., "CFD Verification of Supersonic Retropropulsion for a Central and Peripheral Configuration," IEEEAC Paper 2011-1190, March 2011.

[9] Kleb, B., et. al., "Toward Supersonic Retropropulsion CFD Validation," AIAA Paper 2011-3490, June 2011.

[10] Korzun, A.M., Clark, I.G., and Braun, R.D., "Application of a Reynolds-Averaged Navier Stokes Approach to Supersonic Retropropulsion Flowfields," AIAA Paper 2011-3193, June 2011.

[11] Schauerhamer, D.G., et. al., "Continuing Validation of Computational Fluid Dynamics for Supersonic Retropropulsion," AIAA Paper 2012-0864, January 2012.

[12] Zarchi, K.A., Schauerhamer, D.G., Kleb, W., Carlson, J.-R., and Edquist, K., "Computational Fluid Dynamics Validation and Post-test Analysis of Supersonic Retropropulsion in the Ames 9x7 Unitary Tunnel," AIAA Paper 2012-2705, June 2012.

[13] Hill, J.A.F., and Draper, J.S., "Analytical Approximation for the Flow from a Nozzle into a Vacuum," *Journal of Spacecraft and Rockets*, Vol. 3, No. 10, 1966, pp. 1552-1554. doi: 10.2514/3.28700

[14] Charwat, A.F., "Boundary of Underexpanded Axisymmetric Jets Issuing into Still Air," *AIAA Journal*, Vol. 2, No. 1, 1964, pp. 161-163. doi: 10.2514/3.4159

[15] Finley, P.J., "The Flow of a Jet from a Body Opposing a Supersonic Free Stream," *Journal of Fluid Mechanics*, Vol. 26, No. 2, 1966, pp. 337-368.

[16] Korzun, A.M., *Aerodynamic and Performance Characterization of Supersonic Retropropulsion for Application to Planetary Entry and Descent*, Diss, Georgia Institute of Technology, 2012.

[17] Bakhtian, N.M., and Aftosmis, M.J., "Maximum Attainable Drag Limits for Atmospheric Entry via Supersonic Retropropulsion," 8th International Planetary Probe Workshop, 2011.

[18] Skeen, M.A., *Conceptual Modeling and Analysis of Drag-Augmented Supersonic Retropropulsion for Application in Mars Entry, Descent, and Landing Vehicles*, Thesis, University of Colorado, 2013.

[19] Cordell, C.E. Jr., and Braun, R.D., "Steady State Modeling of Supersonic Retropropulsion Plume Structures," *Journal of Spacecraft and Rockets*, Vol. 50, No. 4, 2013, pp. 763-770. doi: 10.2514/1.A32391
[20] Sibulkin, M., and Gallaher, W.H., "Far-Field Approximation for a Nozzle Exhausting into a Vacuum," *AIAA Journal*, Vol. 1, No. 6, 1963, pp. 1452-1453. doi: 10.2514/3.1835
[21] Van Dyke, M.D., and Gordon, H.D., "Supersonic Flow Past a Family of Blunt Axisymmetric Bodies," NASA TR R-1, October 1958.
[22] Anderson, J.D., *Fundamentals of Aerodynamics*, 4th ed., New York: McGraw-Hill, 2007, pp. 264-273. Print.